HHS Public Access

Author manuscript

Med Phys. Author manuscript; available in PMC 2020 May 01.

Published in final edited form as:

Med Phys. 2019 May ; 46(5): 2251–2263. doi:10.1002/mp.13493.

Systematic analysis of the impact of imaging noise on dual-energy CT-based proton stopping-power-ratio estimation

Hugh HC Lee[1], **Bin Li**[2], **Xinhui Duan**[4], **Linghong Zhou**[3], **Xun Jia**[1], and **Ming Yang**[1,*]

[1]Department of Radiation Oncology, University of Texas Southwestern Medical Center, Dallas, TX 75390, USA

[2]State Key Laboratory of Oncology in South China, Collaborative Innovation Center for Cancer Medicine, Sun Yat-sen University Cancer Center, Guangzhou 510060, China.

[3]Department of Biomedical Engineering, Southern Medical University, Guangzhou, Guangdong 510515, China

[4]Department of Radiology, University of Texas Southwestern Medical Center, Dallas, TX 75390, USA

Abstract

Purpose: Dual-energy CT (DECT) has been shown to have a great potential in reducing the uncertainty in proton stopping-power-ratio (SPR) estimation, when compared to current standard method – the stoichiometric method based on single-energy CT (SECT). However, a few recent studies indicated that imaging noise may have a substantial impact on the performance of the DECT-based approach, especially at a high noise level. The goal of this study is to quantify the uncertainty in SPR and range estimation caused by noise in the DECT-based approach under various conditions.

Methods: Two widely referred parametric DECT methods were studied: the Hünemohr-Saito (HS) method and the Bourque method. Both methods were calibrated using Gammex tissue substitute inserts scanned on the Siemens Force DECT scanner. An energy pair of 80 kVp and 150 kVp with a tin filter was chosen to maximize the spectral separation. After calibrating the model with the Gammex phantom, CT numbers were synthesized using the density and elemental composition from ICRU 44 human tissues to be used as a reference, in order to evaluate the impact of noise alone while putting aside other sources of uncertainty. Gaussian noise was introduced to the reference CT numbers and its impact was measured with the difference between estimated SPR and its noiseless reference SPR. The uncertainty caused by noise was divided into two independent categories: shift of the mean SPR and variation of SPR. Their overall impact on range uncertainty was evaluated on homogeneous and heterogeneous tissue samples of various water equivalent path lengths (WEPL).

*Correspondence: Ming Yang., PhD, Department of Radiation Oncology, UT Southwestern Medical Center, 2280 Inwood Road, Dallas, Texas 75390-9303, Office: 214-648-5057, Fax: 214-648-9533, ming.yang@utsouthwestern.edu.

Conflict of interest

The authors have no conflicts to disclose.

Results: Due to the algorithms being nonlinear and/or having hard thresholds in the CT number to SPR mapping, noise in the CT numbers induced a shift in the mean SPR from its noiseless reference SPR. The degree of the mean shift was dependent on the algorithm and tissue type, but its impact to the SPR uncertainty was mostly small compared to the variation. All mean shifts observed in this study were within 0.5% at a noise level of 2%. The ratio of the influence of variation to mean shift was mostly greater than 1, indicating that variation more likely determined the uncertainty caused by noise. Overall, the range uncertainty (95th percentile) caused by noise were within 1.2% and 1.0% for soft and bone tissues, respectively, at 2% noise with 50 voxels. This value can be considered an upper limit as more voxels and lower noise level rapidly decreased the uncertainty.

Conclusions: We have systematically evaluated the impact of noise to the DECT-based SPR estimation, and identified under various conditions that the variation caused by noise is the dominant uncertainty-contributing component. We conclude that, based on the noise level and tumor depth, it is important to estimate and include the uncertainty due to noise in estimating the overall range uncertainty before implementing a small margin in the range of 1%.

Keywords

stopping-power-ratio (SPR) estimation; dual-energy CT (DECT); random noise; electron density ratio (EDR); effective atomic number (EAN)

1. Introduction

Proton radiotherapy has clear theoretical advantages over conventional photon-based radiotherapy because of its unique dosimetric characteristics known as the Bragg peak. However, the advantages of proton cannot be fully utilized in many cases due to its susceptibility to uncertainties, especially range uncertainty.[1,2] Range uncertainty not only causes healthy tissues to receive unnecessarily high dose because of the extra planning margin, but also can result in sub-optimal beam angle selection (e.g., avoiding ideal beam angles due to critical organs located closely distal to the target). This prevents fully exploiting the high dose gradient at the distal end of the proton beam.

One major source contributing to the range uncertainty is the uncertainty in proton stopping-power-ratio (SPR) estimation. Currently, proton SPR is derived from patient's CT images through a calibration curve. The most widely used method of determining the calibration curve is the stoichiometric method proposed by Schneider *et al*.[3] The major disadvantage of the single calibration curve based method is the degeneracy between CT number and SPR, because these two quantities describe two completely different physical interactions and hence have no one-to-one correspondence. As a result, the single energy CT (SECT)-based method has been shown to be sensitive to potential tissue composition variation between different individuals.[4]

Dual-energy CT (DECT) based approaches have demonstrated their capability of reducing this uncertainty,[5–8] as well as their clinical applicability and relevance to the patient.[9–13] Various methods have been proposed that estimate proton SPR from CT numbers acquired with two different energy spectra. Most methods calculate electron density relative to water

(ρ_e) and effective atomic number (Z) and convert Z to mean excitation energy (I) based on an empirical relationship, followed by calculating SPR using Bethe-Bloch equation with obtained ρ_e and I.[14,15] Han *et al* proposed a method that decomposes the images into two basis materials and calculates SPR based on the proportion of each material.[16] Taasti *et al* proposed a completely empirical approach which fits CT numbers to SPR directly with a predefined function.[17] Most DECT methods have been shown to be robust against tissue composition variation and to achieve uncertainty less than 1% under an ideal condition.[18,19]

In our recent study, we showed that DECT-based methods are particularly susceptible to imaging uncertainty, i.e., a systematic uncertainty (error) in the measured CT number mainly caused by the beam hardening effect.[20] We chose to omit imaging noise in the uncertainty budget because noise was thought to only cause random variation, which will be averaged out in range calculation.[21] However, a recent study by Brousmiche *et al*, which evaluated the impact of imaging noise on SPR estimation for the SECT stoichiometric method, suggested that Gaussian noise may not only cause random variation but also cause systematic error due to the existence of hard thresholds in the calibration curve.[22] Another recent study by Bar *et al* also investigated the impact of imaging noise to the DECT-based methods and compared the performance of DECT-based methods with the SECT-based method under different noise levels.[23] Their study also demonstrated that random imaging noise can cause systematic shift of mean SPR, and pointed out that the DECT-based approach might lose its advantage over the SECT-based approach at a high noise level. However, their conclusion was largely based on an analysis on the error histogram of one particular simulated pelvic CT slice, which has a very specific weight distribution of only a few tissue types and hence is hard to be generalized for the whole population. We believe it is important to evaluate this impact for each individual tissue type and then derive the overall uncertainty estimate based on the weights of each tissue type, i.e., equal weight or weights specific to certain treatment sites. Recently, there has been a few publications experimentally demonstrating with real animal tissues that the DECT methods can achieve range uncertainty of around 1% or less,[5,6,8,24] which makes it even more important to fully understand the impact from imaging noise before applying a tight margin like 1%.

The goal of this study is to systematically evaluate the impact of random imaging noise to the accuracy of the DECT-based SPR estimation. This study used two widely referred parametric DECT methods: the Hünemohr-Saito (HS) method, a generalized method from multiple previous works,[19,20,25,26] and the Bourque method, a method proposed by Bourque *et al*.[18] Questions to be answered through this study include 1) what is the general behavior of the shift of mean SPR for different DECT models; 2) which tissue type suffers the most from this systematic uncertainty, 3) how the impact from the mean shift is compared to that from random variation; and 4) what is a good/robust estimate of the overall impact from imaging noise under different conditions and how it is compared to other uncertainty contributing factors of the DECT approach.

2. Materials and Methods

2.1. DECT-based SPR estimation methods

Many DECT-based methods comprise three steps: 1) estimating EDR (ρ_e) and EAN (Z) from the CT numbers of two energies, 2) converting Z to mean excitation energy (I), and 3) calculating SPR using the Bethe-Bloch formula as

$$\mathrm{SPR} = \rho_e \frac{\ln\frac{2m_e c^2\beta^2}{1-\beta^2} - \beta^2 - \ln I}{\ln\frac{2m_e c^2\beta^2}{1-\beta^2} - \beta^2 - \ln I_w}, \quad (1)$$

where m_e is the rest mass of an electron, c is the speed of light, β is the velocity of proton in vacuum relative to the speed of light, and I_w is the mean excitation energy of water (i.e., 75 eV in this study). In the following section, we briefly describe the two selected calibration-based DECT methods for estimating

ρ_e and Z. Readers can refer to the respective original publication for further details.

2.1.1. The Hunemohr-Saito (HS) method—Saito *et al* proposed a linear regression based method for estimating ρ_e in 2012,[25] which mainly approximates ρ_e as a linear combination of attenuation coefficients (or CT numbers). Later, Hunemohr *et al* used a similar concept to estimate Z.[19] In our previous study, we presented a more generalized model and referred it as the "HS method".[20] The generalized model can be succinctly expressed as

$$\rho_e = a_1 x_L + a_2 x_H + a_3, \text{and} \quad (2)$$

$$\rho_e Z^n = b_1 x_L + b_2 x_H + b_3, \quad (3)$$

where $x_i\,(\forall i = \{\mathrm{L},\mathrm{H}\})$ is the attenuation coefficient of x-ray relative to water $(x = \mu/\mu_w)$, n is the Mayneord's exponent (i.e., approximately in the range [3, 3.3], empirically determined), and a_i and $b_i\,(\forall i = \{1,2,3\})$ are parameters for calibration. Intuitively, the calibration can be viewed as fitting the plane of relative attenuation coefficients to ρ_e followed by $\rho_e Z^n$, both with linear regression.

2.1.2. The Bourque (B) method—Bourque *et al* proposed a polynomial regression based method that uses polynomials of dual-energy index (DEI) or dual-energy ratio (DER) to estimate Z (i.e., defined as Z_{med} in the original publication),[27] followed by polynomials of Z to estimate ρ_e. The equations can be summarized as

$$Z = \sum_{k=1}^{K} c_k \Gamma^{k-1}, \text{and} \quad (4)$$

$$x_i = \rho_{e,i} \sum_{m=1}^{M} b_{m,i} Z^{m-1}, \quad (5)$$

where Γ is either DEI $((x_L - x_H)/x_L + x_H))$ or DER (x_L/x_H), c_k and $b_{m,i}$ are parameters for fitting $(\forall i = \{\text{L,H}\})$, and K and M are polynomial orders that need to be tuned to balance between the accuracy and stability of the algorithm.[18,23] After $\rho_{e,L}$ and $\rho_{e,H}$ are obtained by fitting the equation (Eq. 5), ρ_e is obtained by averaging the two energies as

$$\rho_e = \frac{\rho_{e,L} + \rho_{e,H}}{2}. \quad (6)$$

2.1.3. Z-to-I conversion—ρ_e and Z can be estimated by using one of the DECT-based models mentioned earlier, but to use the Bethe-Bloch equation (Eq. 1) to calculate SPR, I must be obtained. Here we introduce three Z-to-I conversions that were proposed by Yang (Y), Saito (S), and Bourque (B) (Fig. 1).

Yang *et al* proposed an empirical Z-to-I conversion that fits Z to ln I linearly with a threshold at Z=8.5 to separate soft and bone tissues.[28] The fitting can be expressed as

$$\ln I = \begin{cases} C_1 Z + C_2 & Z < 8.5(\text{soft}) \\ C_3 Z + C_4 & Z \geq 8.5(\text{bone}) \end{cases}.$$

Saito *et al* also proposed an empirical Z-to-I conversion similar to Yang's fitting, but differs in that it linearly fits Z^n to ln I instead of Z to ln I, with a threshold at Z=8.78.[26] The fitting can be expressed as

$$\ln I = \begin{cases} C_1 Z^n + C_2 & Z < 8.78(\text{soft}) \\ C_3 Z^n + C_4 & Z \geq 8.78(\text{bone}) \end{cases}. \quad (8)$$

Bourque *et al* proposed using a combination of polynomial and linear fitting to make the fit continuous.[18] Bourque's fitting can be expressed as

$$I = \begin{cases} e_1 Z + e_2 & Z < 6.26 \\ e_3 Z^5 + e_4 Z^4 + e_6 Z^2 + e_7 Z + e_8 & 6.26 \le Z \le 13.52. \\ e_9 Z + e_{10} & Z > 13.52 \end{cases} \quad (9)$$

Hereafter, for simplicity, we will use "ρ_e and Z estimation method + Z-to-I conversion method" to denote a combination for SPR estimation. For example, HS+Y will denote the HS method for ρ_e and Z estimation and the Yang method for Z-to-I conversion.

2.1.4. Model parameters and adjustments—We set n=3.3 for the HS method and K=3 and M=6 for the Bourque method.[20,23] The Z-to-I conversion parameters were calibrated using the ICRU 44 reference human tissues for both methods.[29] A 200 MeV proton beam was assumed when calculating the Bethe-Bloch equation. In addition, we restrained Z as $6<Z<15$ to prevent algorithms from producing negative or complex values of ρ_e, Z, or SPR with noisy CT numbers.

2.2. Data preparation

2.2.1. Calibration—The material inserts provided in Gammex RMI467 phantom (Gammex, Middleton, WI) were used for calibration for both the HS method and the Bourque method, which include LN300, LN450, AP6, BR12, Water, Solid water, SR2, LV1, IB3, B200, CB2–30, CB2–50, and SB3. A small phantom and a large phantom made in-house were scanned with a Siemens SOMATOM Force DECT scanner (Siemens Healthcare, Forchheim, Germany) with 80 kVp and 150 kVp/Sn energy pair.[20] The small phantom mimicking a pediatric patient was circular with a diameter of 16 cm and the large phantom mimicking an adult patient was ellipsoidal with a semi-major axis of 40 cm and a semi-minor axis of 28 cm. Both phantoms were scanned using clinical DE AP protocol with automatic exposure control (AEC). The scan was in helical mode with 5 mm slice thickness and 0.6 pitch. For the small phantom, the average tube current time product was 9.5 mAs and 8.5 mAs for 80 kVp and 150 kVp/Sn, respectively, with a display field-of-view (DFOV) of 200 mm. For the large phantom, the average tube current time product was 358 mAs and 74 mAs for 80 kVp and 150 kVp/Sn, respectively, with a DFOV of 450 mm. Reconstruction kernel was Bf44 with iterative reconstruction strength 3. A 10 mm diameter region of interest (ROI) was drawn in the middle of the insert to obtain the mean CT number of the insert, and CT numbers from the small phantom and the large phantom were averaged to obtain the mean CT number for each insert. These mean CT numbers and the reference ground truth ρ_e, Z, and SPR were used to calibrate each method. Calibrated parameters are shown in Table 1.

The Z-to-I conversion parameters C_i and e_i can be calibrated using reference human tissue data such as ICRU 44. We used the same parameters used in the original publication by Li *et al* and Bourque *et al*.[18,20] with Yang's fitting values as C_1=0.1196, C_2=3.4078, C_3=0.1033, and C_4=3.2929. For Saito's fitting, we used ICRU 44 instead of ICRU 46 (Saito's original publication) and obtained fitting values as C_1=2.8578E-04, C_2=4.0762, C_3=1.0340E-04, and C_4=4.1478.[26]

2.2.2. Data for evaluation—To analyze the impact of noise alone and negate other sources of uncertainty, reference CT numbers and SPRs were calculated from ICRU 44 'reference' human tissues using their elemental composition. As the DECT methods take two CT numbers as the input and produces ρ_e and Z as the two outputs, it is possible to reverse the calculation and obtain two CT numbers from ρ_e and Z. By using this approach, reference CT numbers were directly mapped to reference SPRs without error. Introducing noise to the reference CT numbers enabled us to solely analyze the impact of noise without considering other uncertainties. With the elemental composition and mass density, relative attenuation coefficients for the HS method were obtained as

$$\hat{x}_{L,HS} = \frac{\rho_e(Z^n a_2 - b_2) - a_2 b_3 + a_3 b_2}{a_2 b_1 - a_1 b_2}, \text{and} \quad (10)$$

$$\hat{x}_{H,HS} = \frac{\rho_e(Z^n a_1 - b_1) - a_1 b_3 + a_3 b_1}{a_1 b_2 - a_2 b_1}, \quad (11)$$

Similarly, for the Bourque method with K=3, $\hat{\Gamma}$ was obtained using the quadratic formula as

$$\hat{\Gamma} = \frac{-c_2 + \sqrt{c_2^2 - 4c_3(c_1 - Z)}}{2c_3}, \quad (12)$$

and relative attenuation coefficients as

$$\hat{x}_{L,BQ} = \frac{2\rho_e(\sum_{m=1}^{M} b_{m,1} Z^{m-1} \sum_{m=1}^{M} b_{m,2} Z^{m-1})}{\sum_{m=1}^{M} b_{m,2} Z^{m-1} + \frac{1-\hat{\Gamma}}{1+\hat{\Gamma}} \sum_{m=1}^{M} b_{m,1} Z^{m-1}}, \quad (13)$$

and

$$\hat{x}_{H,BQ} = \frac{1-\hat{\Gamma}}{1+\hat{\Gamma}} \hat{\mu}_{1,BQ}. \quad (14)$$

For each of the two methods, CT numbers calculated with the corresponding method were used to evaluate the impact of noise. Reference CT numbers are summarized in Table 2. Note that all CT numbers presented in this paper are shifted CT numbers that is +1000 from the original HU definition (i.e., HU=1000x/x_w). This way, the relative change of HU is directly proportional to the change of linear attenuation coefficient.

To diversify the 'reference' tissues for our test, the ICRU 44 'reference' human tissues were given variations in mass density, as well as hydrogen and calcium percentage for soft and bone tissues, respectively, to account for compositional variations among individuals.[4] 2000 'individualized' human tissue samples generated this way had CT numbers slightly deviated from the ICRU 44 'reference' human tissue samples. This dataset covers a wider patient population and helps to reach a more generalized conclusion.

To validate that our calculated CT numbers closely represent real CT numbers, we compared the calculated and measured CT numbers of the tissue substitute inserts (Fig. 2). For CT numbers calculated with the HS method, the RMS difference of 80 kVp was 7.17 HU and 19.91 HU for soft and bone tissues, respectively, and the RMS difference of 150 kVp/Sn was 4.11 HU and 4.16 HU for soft and bone tissues, respectively. For CT numbers calculated with the Bourque method, the RMS difference of 80 kVp was 6.96 HU and 11.22 HU for soft and bone tissues, respectively, and the RMS difference of 150 kVp/Sn was 7.79 HU and 6.68 HU for soft and bone tissues, respectively. These differences demonstrated the 'imperfectness' of the DECT model, which were categorized as the modeling uncertainty in our previous study.[20]

2.3. Evaluation of the impact of noise

Throughout the paper, we mainly used HS+Y (HS method with Yang's Z-to-I conversion) and B+B (Bourque method with Bourque's Z-to-I conversion) to evaluate the impact of noise to these originally proposed algorithms. This way the results are consistent with our previous work and can be directly referred to.[20] Only at the end of the study we compared different combinations of "ρ_e and Z estimation" and "Z-to-I conversion" to identify the dependence of two steps.

Two components that arise from the noise, i.e., the shift of mean SPR and the variation of SPR, were individually analyzed to gauge each of their impact. The shift of mean SPR can be regarded as a measure of the accuracy of SPR estimation because it measures the systematic error. The variation of SPR, on the other hand, serves as a measure of the precision of SPR estimation because it measures the random error (fluctuation). The degree of mean shift is dependent on the nonlinear components (i.e., hard thresholds and nonlinear curvatures) in the CT number to SPR mapping. The degree of variation is dependent on the steepness of the slope in the mapping. These two constitute the SPR uncertainty caused by noise.

For a given pair of reference CT numbers, 100k samples with Gaussian random noise of a specified percentage were generated. The noise was applied to either HU_L,HU_H, or both (uncorrelated between HU_L and HU_H) to identify the impact of low and high energy CT numbers independently. This way we were able to identify which of the two energies (i.e., 80 kVp or 150 kVp/Sn) had a larger impact on SPR estimation under the same noise level. This can provide additional information when the noise ratio between low and high energy pair is not exactly one as considered in this study, and may help optimizing the imaging dose by adjusting the noise ratio. With these samples, the mean shift was calculated as the difference from the mean of the SPR to the SPR of the mean CT numbers, expressed as

$$\Delta \mathrm{SPR}\,(\%) = \frac{\overline{\mathrm{SPR}} - \mathrm{SPR}|_{x_i = \bar{x}_i}}{\mathrm{SPR}|_{x_i = \bar{x}_i}} \times 100, \quad (15)$$

where $\overline{\mathrm{SPR}}$ is the mean of SPR, and $\mathrm{SPR}|_{x_i = \bar{x}_i}$ $(\forall i = \{\mathrm{L,H}\})$ is the SPR of the mean CT number. The variation was evaluated as the standard deviation of the SPR relative to the shifted mean, expressed as

$$\sigma_{\mathrm{SPR}}(\%) = \frac{std(\mathrm{SPR})}{\overline{\mathrm{SPR}}} \times 100. \quad (16)$$

The mean shift and variation were assessed for each tissue. Tissues were grouped into soft and bone tissue and root-mean-squared error (RMSE) was taken for each group for group-wise assessment. This result reflects the uncertainty due to noise in an individual voxel for a specific tissue type.

To evaluate the overall impact of noise on range uncertainty, the number of voxels and tissue heterogeneity were considered to estimate its realistic impact. Uncorrelated Gaussian noise was added to 50, 100, or 300 voxels (i.e., 5, 10, and 30 cm with 1mm/pixel resolution) of homogeneous or heterogeneous tissues for both HU_L and HU_H. For homogeneous tissues, each of the 34 tissues were evaluated individually and RMS was taken to derive the group average for soft and bone tissues separately. For heterogeneous tissues, each voxel was first assigned to a particular tissue group and then a random tissue was drawn from that particular group with uniform probability to fill that voxel. The number of voxels assigned to each tissue group was based on the weight of that specific tissue group for a specific tumor site. The weight of each tissue group was calculated by dividing the water-equivalent-pathlength (WEPL) by the average SPR of each tissue group and renormalized (i.e., $\text{Voxel weight} = (\mathrm{WEPL}_i/\mathrm{SPR}_i)/\sum(\mathrm{WEPL}_i/\mathrm{SPR}_i)$, where i is the lung, soft, and bone tissue).

Three tumor sites, i.e., prostate, lung, and head-and-neck (HN) were considered in study. Table 3 lists the WEPL weights of lung, soft and bone tissue groups for each tumor site used in this study, which was based on our previous studies.[4,20] 100,000 samples were simulated for both homogeneous and heterogeneous tissues to calculate the 95$^{\mathrm{th}}$ percentile. In this study, the notion of 95$^{\mathrm{th}}$ percentile and 2σ were used interchangeably for simplicity.

3. Results

3.1 Behavior of the DECT methods in the presence of Gaussian noise

We have calculated and plotted the parameters (ρ_e, Z, and SPR) for all possible CT number combinations within the range [0, 3000] (Fig. 3), which covers the CT number range of a typical patient CT dataset. This was used to obtain an overall picture of the DECT model behavior, especially the possible non-linearity and hard thresholds existing in the DECT calculations. In generating this plot, we found negative and complex values in Z calculation

for both methods, which produced large errors. Because of this, we decided to implement the regularization of $6<Z<15$ in our calculation. This improved the stability of both methods in the presence of noise.

The main difference between these two methods existed in the ρ_e map; the CT number-to-ρ_e map of the HS method was linear while that of the Bourque method was not. In the HS method, ρ_e was calculated first with a linear combination of HU_L and HU_H, independent of Z, so the calculated ρ_e fell on a perfect linear plane for all HU combinations, except for the values near boundaries where ρ_e was forced to zero to avoid negative values. On the contrary, in the Bourque method, Z was calculated first and then ρ_e was calculated based on Z (Eq. 4, 5, and 6), so the non-linear curvature and the regularization used in Z calculation are passed onto ρ_e. The CT number-to-SPR map resembles the ρ_e map closely for both methods, due to the dominance of ρ_e in the SPR calculation. The overall SPR distribution of the HS+Y method appears more linear than that of the B+B method.

Because the nonlinear regions relevant to the tissue of interest were not clearly visible in the 3-D plot in Fig. 3, we plotted line profiles of SPR around an example tissue (adipose) to better illustrate the hard thresholds and non-linear curvatures in the SPR estimation (Fig. 4). Two hard thresholds were observed for the HS+Y method, whereas one hard threshold was observed for the B+B method. The hard threshold visible in both methods was caused by the regularization of $6<Z<15$. The other hard threshold only visible in the HS+Y method was $Z_{th}=8.5$ for separating soft and bone tissues in the Z-to-I conversion. The polynomial function used in the Bourque's Z-to-I conversion produced a smooth transition from soft to bone tissues, which prevented an abrupt change of SPR near the boundary.

Fig. 5 shows the distribution of SPR in the presence of Gaussian noise, which became asymmetric due to the nonlinearities shown in Figs. 3 and 4. The asymmetric SPR distribution created a difference between the SPR of the mean CT number (black solid lines) and the mean of the SPR (red dashed lines), which is the root cause of the shift of mean SPR. The shift of mean SPR increased with the noise level, as a larger proportion of CT numbers were affected by the nonlinear regions. Similar shift of mean SPR was also reported by Brousmiche *et al* for the SECT stoichiometric method and Bar *et al* for DECT methods. Their magnitudes were reported to vary depending on the algorithm, tissue type, and noise level.[22,23] Unlike the SPR variation due to noise, the mean shift impacts the SPR systematically and cannot be mitigated by averaging a number of voxels.

3.2. Uncertainties due to noise: mean shift and variation

Fig. 6 visualizes the degree of SPR mean shift for each combination of of HU_L and HU_H. The regions covered by 'reference' human tissues and 'invidualized' human tissues were highlighted with markers and shades. For the HS+Y method, soft tissues were predominantly affected by the hard thresholds caused by the Z-to-I conversion line located lower right from most soft tissues and $Z>6$ regularization line located upper left from most soft tissues, as also seen in Fig. 4. Bone tissues, on the other hand, had a small mean shift because no hard thresholds or non-linearity existed nearby. For the B+B method, soft tissues were only affected by the $Z>6$ regularization line, but the degree was much smaller than that of the Z-to-I conversion line of the HS+Y method. Unlike the HS+Y method, bone tissues

experienced a nonlinear curvature in the B+B method, although the degree was small as the cortical bone with the largest mean shift still had less than 0.5% mean shift at 5% noise.

Fig. 7 shows the distribution of the mean shift for 'individualized' tissue populations in the presence of 2% imaging noise. For the HS+Y method, some soft tissues had a high mean shift (c.f., thyroid was the highest with 1.34%) but bone tissues only had a sharp peak near zero because bone tissues were far away from the nonlinear regions as seen in Fig. 6. For the B+B method, we saw an opposite result as soft tissues had smaller mean shift than bone tissues. The high mean shift of the HS+Y method for thyroid is not surprising as thyroid had a mean Z=8.41 that is close to the threshold of Z_{th}=8.5 employed in Yang's Z-to-I conversion.

The magnitude of SPR mean shift for soft and bone tissues are shown as a function of noise level in Fig. 8 (a). Noise was added to either HU_L, HU_H, or both to specify the contribution from each of the two energies. For the HS+Y method, soft tissues had mean shifts of 0.47% at 2% noise and 0.90% at 5% noise, which were much higher than those of bone tissues: 0.02% at 2% noise and 0.12% at 5% noise. For the B+B method, soft tissues had mean shifts of only 0.04% at 2% noise and 0.54% at 5% noise. Bone tissues had higher mean shifts of 0.07% at 2% noise and 0.41% at 5% noise. The growth of mean shift was observed to be an exponential function of noise level except for the soft tissue group with the HS+Y method, putatively due to the influence from double hard thresholds with opposite sign cancelling out each other. For both methods, HU_L and HU_H contributed with a similar degree to the mean shift.

The standard deviation (i.e., variation) of SPR for soft and bone tissues are also shown as a function of noise level (Fig. 8 (b)). Both methods showed a similar trend and similar values for soft and bone tissues. The degree of variation of SPR has been previously shown to be linearly proportional to the variation of CT numbers.[20,21,30] Unlike the mean shift, however, the varation was dominated by HU_H, shown by the fact that adding noise only to HU_H and to both HU_L and HU_H showed a similar degree of variation.[20]

3.3. Range uncertainty due to noise in homogeneous/heterogeneous tissues

Due to the stochastic nature of the random variation, its overall impact to the range uncertainty depends on the number of samples. Thus, scenarios with varying number of voxels and tissue heterogeneity were studied to estimate the overall range uncertainty.

Fig. 9 (a) plots the range uncertainty (95^{th} percentile or 2σ) caused by the imaging noise, including the contribution from both the mean shift and the random variation. Since the range uncertainty caused by the variation depends on the number of voxels (tumor depth), we considered three scenarios with homogeneous tissue samples comprising 50, 100, or 300 voxels. The range uncertainty increased with the noise level for both methods and both tissue groups. However, the HS+Y method produced a larger range uncertainty for soft tissues than the B+B method, while both methods showed similar range uncertainty for bone tissues.

To further compare the relative impact of the mean shift and variation, we plotted the ratio of the overall range uncertainty caused by the variation to that by the mean shift in Fig. 9 (b). As expected, we found the ratio of variation to mean shift decreases as the number of voxels increases. In addition, we found this ratio decreases rapidly as the noise level increases, which indicates that the mean shift increases faster than the variation, except for the HS+Y method when applied to soft tissues. It is also seen in Fig. 9 (b) that the ratio of variation to mean shift is substantially larger than 1 under most conditions for both methods, except for the combination of 300 voxels of soft tissues with the HS+Y method which had a ratio slightly smaller than 1. This indicates that the systematic shift only exist in certain conditions and the stochastic variation is usually the dominant uncertainty contributing factor in most conditions.

To confirm the trend seen with homogeneous tissues, we also estimated the range uncertainty (2σ) for heterogeneous tissues for three different tumor sites (Table 4). We chose 50 voxels to demonstrate a worst-case scenario which will result in the largest overall range uncertainty among studied conditions. Even though multiple different tissues were arbitrarily distributed within a set of 50 voxels, averaging effect still came into play for variation, effectively reducing the range uncertainty in a similar manner as for homogeneous tissues. As the soft tissue was the greatest contributor for all three tumor sites, the range uncertainty (2σ) for heterogeneous tissues were close to that of homogeneous soft tissues. In a realistic condition of 2% noise, the RMSE of three tumor sites was 1.10% with the HS+Y method and 0.83% with the B+B method, which were between the values of homogeneous soft and bone tissues but closer to the soft tissue value.

3.4. Comparison of HS+Y and B+B to other combinations of methods

We also investigated different combinations of "ρ_e and Z estimation" and "Z-to-I conversion" on SPR mean shift and variation to study the dependence between these two steps (Fig. 10). It is seen that there is a substantial difference in the mean shift among different combinations. By contrast, the variation was rather stable for a given ρ_e and Z estimation method. We can confirm that the degree and location of hard thresholds impacts the mean shift largely, but not the variation. The HS+Y method had the largest mean shift among the combinations we tested, whereas the variations were rather comparable for any HS or B method.

4. Discussion

In this study, we have systematically evaluated the impact of noise on SPR estimation with the DECT algorithms for a generalized tissue population. We evaluated noise as the sole source of uncertainty while leaving aside other uncertainties in order to investigate the impact of noise alone. To make our estimate more robust, we have included more possible CT number pairs by introducing additional tissue composition variation to the 'reference' human tissues. In addition, we separated the impact from the mean shift and the variation, and were able to demonstrate that the variation component is the dominant contributing factor under most conditions for the two DECT methods implemented in this study. The only exception happened when the tumor was at a deep depth (~30 cm), in which case the

mean shift was only slightly larger than the variation with the HS+Y method. Moreover, we estimated the overall range uncertainty for both homogeneous and heterogeneous tissues. Similar uncertainty values were observed for these two groups, which supports that the averaging effect is still in play regardless of tissue heterogeneity.

The regularization $6<Z<15$ employed in this study was not described in the original studies,[18,20] but this was necessary in order to prevent both algorithms from producing unrealistic values (complex or negative number) with added noise. Especially given that these algorithms involve polynomial or exponential fitting to estimate Z, the value of Z can be distorted substantially with an abnormal combination of CT numbers, which were relieved by setting $6<Z<15$. Although this created an additional hard threshold in the CT number-to-SPR mapping, the overall stability and accuracy were improved with noisy CT numbers.

The HS+Y method showed a larger mean shift than the B+B method for the soft tissue group. We found that the mean shift is sensitive to the specific implementation such as the selection of Z-to-I conversion and the selection of specific regularization on Z (no regularization v.s. $Z>6$ v.s. $Z>0$). Possible measures can be taken to reduce the mean shift for the HS+Y method. Among different combinations we have tried with the HS method, Saito's Z-to-I conversion method yielded the smallest mean shift (Fig. 10). This HS+S method reduced the mean shift due to noise mainly by linearizing the CT number-to-SPR mapping (by substituting $\ln I$ with Z^n in the Bethe-Bloch equation[26]). The use of hard threshold, however, may still be problematic when a large chunk of soft and bone tissue mixture exists near the threshold.[31] With knowing these, we did not apply any adjustments to the original HS+Y methods because the scope of this study was to estimate the baseline of the impact of noise.

Unlike the mean shift, SPR random variation stayed relatively consistent among all tissue types within the same tissues group. It was largely due to the fact that SPR variation mainly depends on the slope of the mapping of CT number-to-SPR.[20,21,30] For both the HS+Y method and the B+B method, HU_H was much more influential than HU_L in estimating the SPR (Fig. 8 (b)) because the slope of HU_H to SPR was steeper (Fig. 4). This suggests the possibility of optimizing the ratio of mAs between low and high energy CT scans to minimize the total SPR variation under the same amount of total imaging dose, which may be worthwhile to look into in the future.

Our evaluation with heterogeneous tissues produced a similar range uncertainty as that of homogeneous tissues. As expected, the values were closer to that of the soft tissue group because soft tissues take up more than 60–80% of the total weight of each of the three tumor sites (Table 3). The averaging effect was also present in heterogeneous tissues. For a sum of Gaussian random variables $\sum_i X_i$ where X_i are independent Gaussians, the standard deviation relative to the mean is $\sqrt{\sum_i \sigma_i^2} / \sum_i \bar{X}_i$, where σ_i is the standard deviation of X_i. This value decreases as the number of X_i (i.e., number of voxels) increases regardless of the identicalness of X_i (i.e., homogeneity of tissues) (c.f., if X_i are identical then $\sum_i X_i$ becomes Gaussian according to the central limit theorem). With nonlinearities the distribution of SPR

is no longer Gaussian but the distribution is still fairly symmetrical with both positive and negative values. Because of that, the standard error would still decrease as the number of samples increases. Our test can also be performed on other heterogeneous samples with a different tissue distribution than what is used in this study, but the result is not likely to change much because only certain tissues (e.g., thyroid and cartilage with the HS+Y method) had a large mean shift and the rest had a similarly small mean shift and variation within each tissue group.

The root-sum-square (RSS) calculation is a standard way to combine the uncertainties from different uncorrelated sources to derive a single value representing the total uncertainty.[20] Because of the nature of the RSS calculation, the largest uncertainty usually dominates over other smaller uncertainties. Therefore, the ultimate impact of noise to the total range uncertainty depends on its relative magnitude compared to other uncertainty factors. Our recent study showed that the total range uncertainty without considering noise were 2.4% and 4% (2σ) for the soft and bone tissue group, respectively.[20] If the additional uncertainty due to noise at a 2% noise level for a tumor at 5 cm depth (a worst case scenario) is considered, the total uncertainty becomes 2.52% and 4.10% for the soft and bone tissue group, respectively, which is only a marginal increase of 0.12% and 0.10%. However, a few recent experimental validation studies using DECT reported the overall range uncertainty to be around 1% or less.[5,8] If 1% were assumed as the range uncertainty for both the soft and bone tissue groups, the total uncertainty after including the noise becomes 1.52% and 1.37% for the soft and bone tissue group, respectively, which is a decent increase of 0.52% and 0.37%. This suggests that the impact from noise should be well evaluated based on the noise level seen in patient CT images and the tumor depth, before implementing a small treatment margin (~1%) for range uncertainty in the clinic.

One drawback of this study is that only two methods were selected in this study. We did not implement other existing DECT algorithms because it was not our goal to compare different methods and reach a general conclusion which method is more superior. Although B+B method was more robust to noise than HS+Y method, our main focuses is to establish a framework for estimating the impact of Gaussian noise so that any center can do their own estimate for their selected DECT algorithm.

5. Conclusion

We have systematically evaluated the impact of noise on SPR estimation using two parametric DECT methods. Mean shift and variation of SPR due to noise were thoroughly investigated as to how they constitute the SPR uncertainty. DECT methods with hard thresholds suffered the most from the mean shift, and the mean shift was mostly observed in soft tissues. Nonetheless, the impact of mean shift was relatively small compared to the random variation caused by the noise, except for a certain method and tissue type. Range uncertainty due to noise was approximately 1% (2σ or 95th percentile) at 2% noise level and 2.5% at 5% noise level. Compared to the uncertainty of 2.4% (soft) and 4% (bone) caused by other factors low noise is not a major concern. However, if we were to implement a small margin of 1% for the proton range, it is important to estimate and include the uncertainty due to noise. By knowing how much impact the noise can make among other SPR

uncertainties, future studies will be able to focus on decreasing the uncertainty that is most influential to the range estimation.

Acknowledgments

We thank Parkland Hospital for granting access to the Siemens SOMATOM Force DECT scanner. This work was partially supported by the Cancer Prevention and Research Institute of Texas grant (RP160661), NIH grant (P20CA183639–01A1), National Natural Science Foundation of China (No. 81571771), and Ministry of Science and Technology of China (No. 2015BAI01B10).

Reference

1. Baumann M, Krause M, Overgaard J, et al. Radiation oncology in the era of precision medicine. Nat Rev Cancer 2016;16(4):234–249. [PubMed: 27009394]
2. Bortfeld TR, Loeffler JS. Three ways to make proton therapy affordable. Nature 2017;549(7673): 451–453. [PubMed: 28959981]
3. Schneider U, Pedroni E, Lomax A. The calibration of CT Hounsfield units for radiotherapy treatment planning. Phys Med Biol 1996;41(1):111–124. [PubMed: 8685250]
4. Yang M, Zhu XR, Park PC, et al. Comprehensive analysis of proton range uncertainties related to patient stopping-power-ratio estimation using the stoichiometric calibration. Phys Med Biol 2012;57(13):4095–4115. [PubMed: 22678123]
5. Mohler C, Russ T, Wohlfahrt P, et al. Experimental verification of stopping-power prediction from single- and dual-energy computed tomography in biological tissues. Phys Med Biol 2018;63(2).
6. Taasti VT, Michalak GJ, Hansen DC, et al. Validation of proton stopping power ratio estimation based on dual energy CT using fresh tissue samples. Phys Med Biol 2018;63(1).
7. Wohlfahrt P, Mohler C, Richter C, Greilich S. Evaluation of Stopping-Power Prediction by Dual- and Single-Energy Computed Tomography in an Anthropomorphic Ground-Truth Phantom. Int J Radiat Oncol 2018;100(1):244–253.
8. Bar E, Lalonde A, Zhang RX, et al. Experimental validation of two dual-energy CT methods for proton therapy using heterogeneous tissue samples. Med Phys 2018;45(1):48–59. [PubMed: 29134674]
9. Hudobivnik N, Schwarz F, Johnson T, et al. Comparison of proton therapy treatment planning for head tumors with a pencil beam algorithm on dual and single energy CT images. Med Phys 2016;43(1):495–504. [PubMed: 26745942]
10. Wohlfahrt P, Mohler C, Hietschold V, et al. Clinical Implementation of Dual-energy CT for Proton Treatment Planning on Pseudo-monoenergetic CT scans. Int J Radiat Oncol 2017;97(2):427–434.
11. Wohlfahrt P, Mohler C, Stutzer K, Greilich S, Richter C. Dual-energy CT based proton range prediction in head and pelvic tumor patients. Radiother Oncol 2017;125(3):526–533. [PubMed: 29050953]
12. Wohlfahrt P, Troost EGC, Hofmann C, Richter C, Jakobi A. Clinical Feasibility of Single-Source Dual-spiral 4D Dual-Energy CT for Proton Treatment Planning Within the Thoracic Region. Int J Radiat Oncol 2018;102(4):830–840.
13. Taasti VT, Muren LP, Jensen K, et al. Comparison of single and dual energy CT for stopping power determination in proton therapy of head and neck cancer. Physics and Imaging in Radiation Oncology 2018;6:14–19.
14. van Elmpt W, Landry G, Das M, Verhaegen F. Dual energy CT in radiotherapy: Current applications and future outlook. Radiother Oncol 2016;119(1):137–144. [PubMed: 26975241]
15. Möhler C, Wohlfahrt P, Richter C, Greilich S. On the equivalence of image-based dual-energy CT methods for the determination of electron density and effective atomic number in radiotherapy. Physics and Imaging in Radiation Oncology 2018;5:108–110.
16. Han D, Siebers JV, Williamson JF. A linear, separable two-parameter model for dual energy CT imaging of proton stopping power computation. Med Phys 2016;43(1):600–612. [PubMed: 26745952]

17. Taasti VT, Petersen JBB, Muren LP, Thygesen J, Hansen DC. A robust empirical parametrization of proton stopping power using dual energy CT. Med Phys 2016;43(10):5547–5560. [PubMed: 27782721]

18. Bourque AE, Carrier JF, Bouchard H. A stoichiometric calibration method for dual energy computed tomography. Phys Med Biol 2014;59(8):2059–2088. [PubMed: 24694786]

19. Hunemohr N, Krauss B, Tremmel C, Ackermann B, Jakel O, Greilich S. Experimental verification of ion stopping power prediction from dual energy CT data in tissue surrogates. Phys Med Biol 2014;59(1):83–96. [PubMed: 24334601]

20. Li B, Lee HC, Duan X, et al. Comprehensive analysis of proton range uncertainties related to stopping-power-ratio estimation using dual-energy CT imaging. Phys Med Biol 2017;62(17): 7056–7074. [PubMed: 28678019]

21. Chvetsov AV, Paige SL. The influence of CT image noise on proton range calculation in radiotherapy planning. Physics in Medicine & Biology 2010;55(6):N141. [PubMed: 20182006]

22. Brousmiche S, Souris K, de Xivry JO, Lee JA, Macq B, Seco J. Combined influence of CT random noise and HU-RSP calibration curve nonlinearities on proton range systematic errors. Phys Med Biol 2017;62(21):8226–8245. [PubMed: 28817383]

23. Bar E, Lalonde A, Royle G, Lu HM, Bouchard H. The potential of dual-energy CT to reduce proton beam range uncertainties. Med Phys 2017;44(6):2332–2344. [PubMed: 28295434]

24. Xie YH, Ainsley C, Yin LS, et al. Ex vivo validation of a stoichiometric dual energy CT proton stopping power ratio calibration. Phys Med Biol 2018;63(5).

25. Saito M Potential of dual-energy subtraction for converting CT numbers to electron density based on a single linear relationship. Med Phys 2012;39(4):2021–2030. [PubMed: 22482623]

26. Saito M, Sagara S. Simplified derivation of stopping power ratio in the human body from dual-energy CT data. Med Phys 2017.

27. Johnson T, Fink C, Schönberg SO, Reiser MF. Dual energy CT in clinical practice Springer Science & Business Media; 2011.

28. Yang M, Virshup G, Clayton J, Zhu XR, Mohan R, Dong L. Theoretical variance analysis of single- and dual-energy computed tomography methods for calculating proton stopping power ratios of biological tissues. Phys Med Biol 2010;55(5):1343–1362. [PubMed: 20145291]

29. White DR, Booz J, Griffith RV, Spokas JJ, Wilson IJ. Tissue substitutes in radiation dosimetry and measurement. ICRU Report 44 1989. doi: 10.1093/jicru/os23.1.Report44.

30. Yang M, Virshup G, Clayton J, Zhu XR, Mohan R, Dong L. Does kV-MV dual-energy computed tomography have an advantage in determining proton stopping power ratios in patients? Phys Med Biol 2011;56(14):4499–4515. [PubMed: 21719949]

31. Mohler C, Wohlfahrt P, Richter C, Greilich S. Range prediction for tissue mixtures based on dual-energy CT. Phys Med Biol 2016;61(11):N268–N275. [PubMed: 27182757]

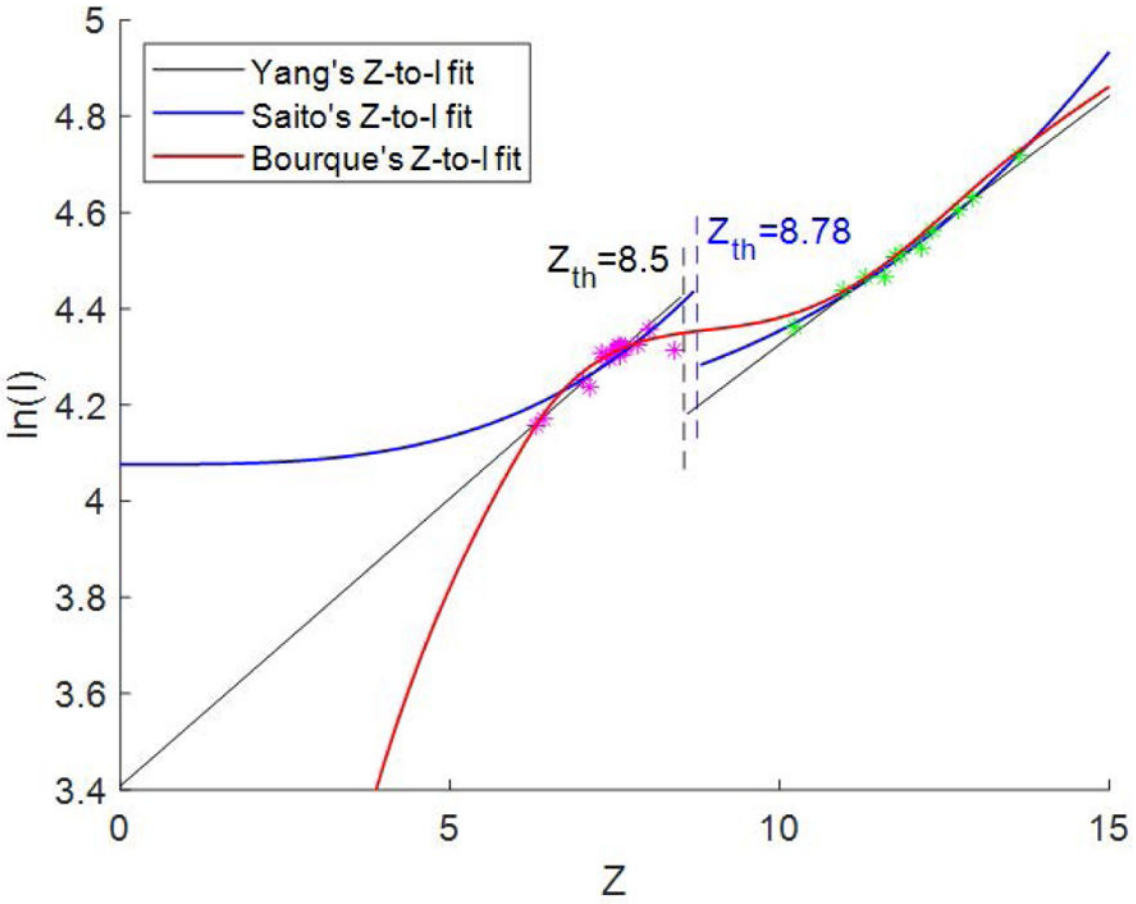

Figure 1.

Z-to-*I* conversions proposed by Yang (Y), Saito (S), and Bourque (B). All three methods were fitted using the ICRU 44 reference human tissues. Magenta asterisks indicate soft tissues and green asterisks indicate bone tissues.

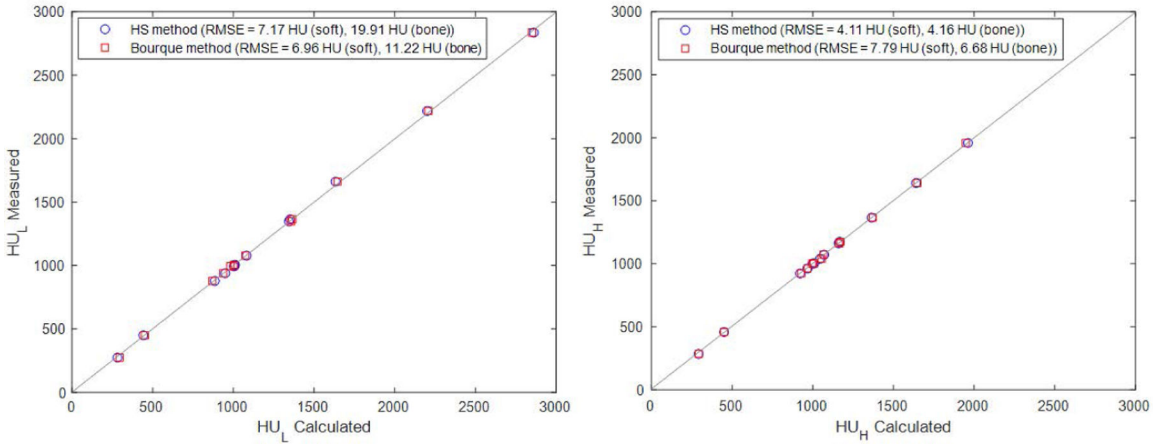

Figure 2.

Calculated vs. measured CT numbers of the Gammex phantom inserts using the HS method (circle) and the Bourque method (square) for HU_L (left) and HU_H (right). A 45° line (gray) is drawn as a reference.

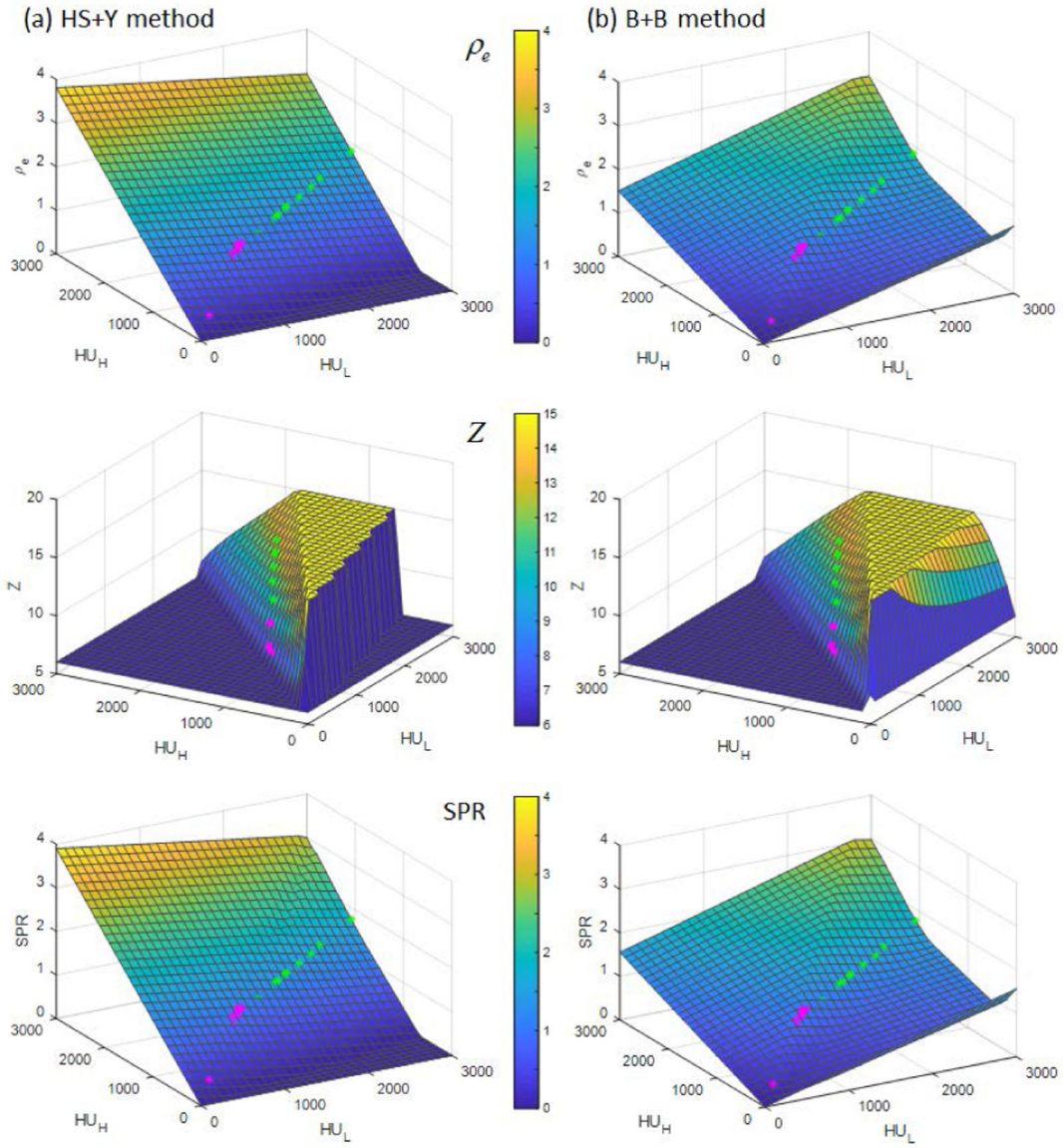

Figure 3.

ρ_e, Z, and SPR of (a) the HS+Y method and (b) the B+B method with all the possible combinations of CT numbers within [0, 3000] with grid size of 100. Magenta and green asterisks represent soft tissues and bone tissues, respectively, selected from ICRU 44 (Table 2). Note that all negative or complex values were forced to zero and Z was regularized to [6, 15] to avoid unrealistic values.

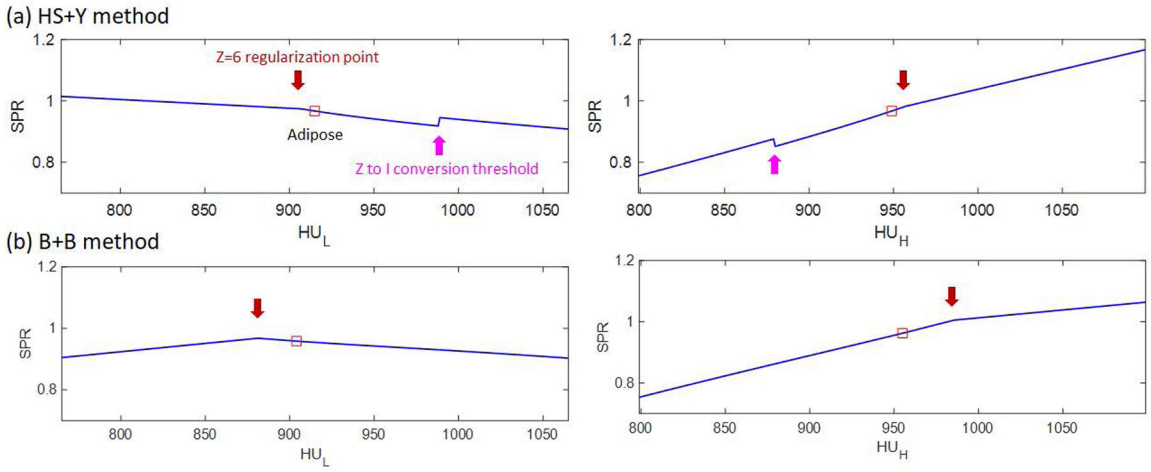

Figure 4.

Demonstration of the nonlinearities existing in the CT number to SPR map for (a) the HS+Y method and (b) the B+B method, respectively. Adipose tissue was selected here as an example. Red squares indicate the reference CT numbers of adipose.

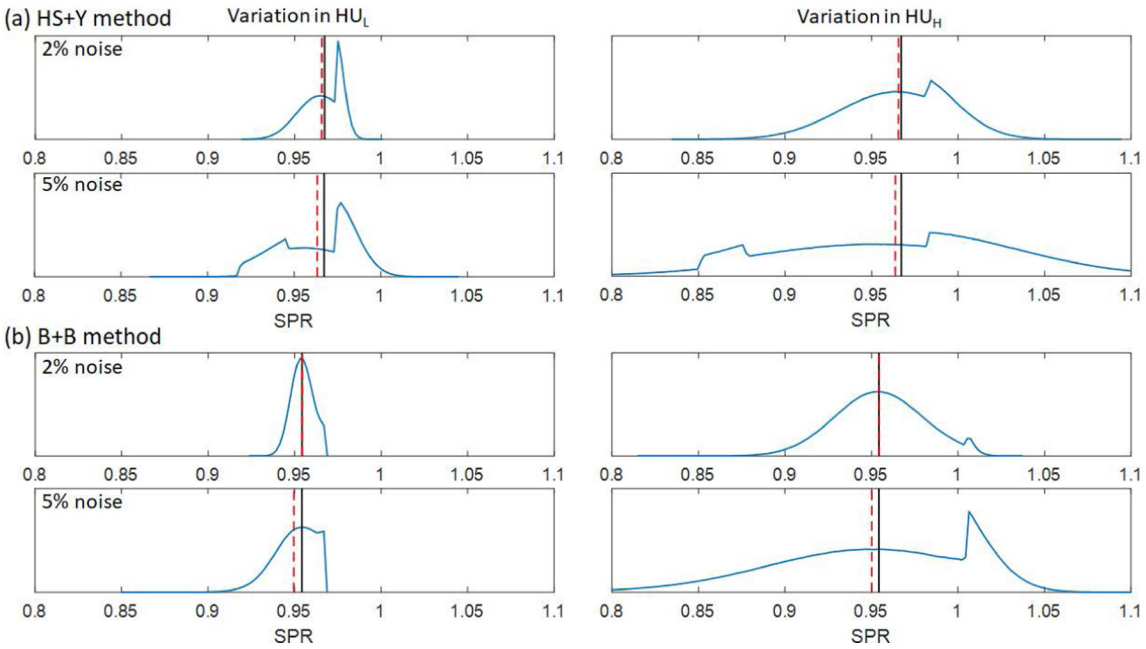

Figure 5.

SPR distribution of a soft tissue (adipose) at 2% and 5% noise in HU_L and HU_H for (a) the HS+Y method and (b) the B+B method, respectively. Black solid lines indicate the SPR of the mean CT numbers (i.e., reference SPR) and red dashed lines indicates the mean of the SPR.

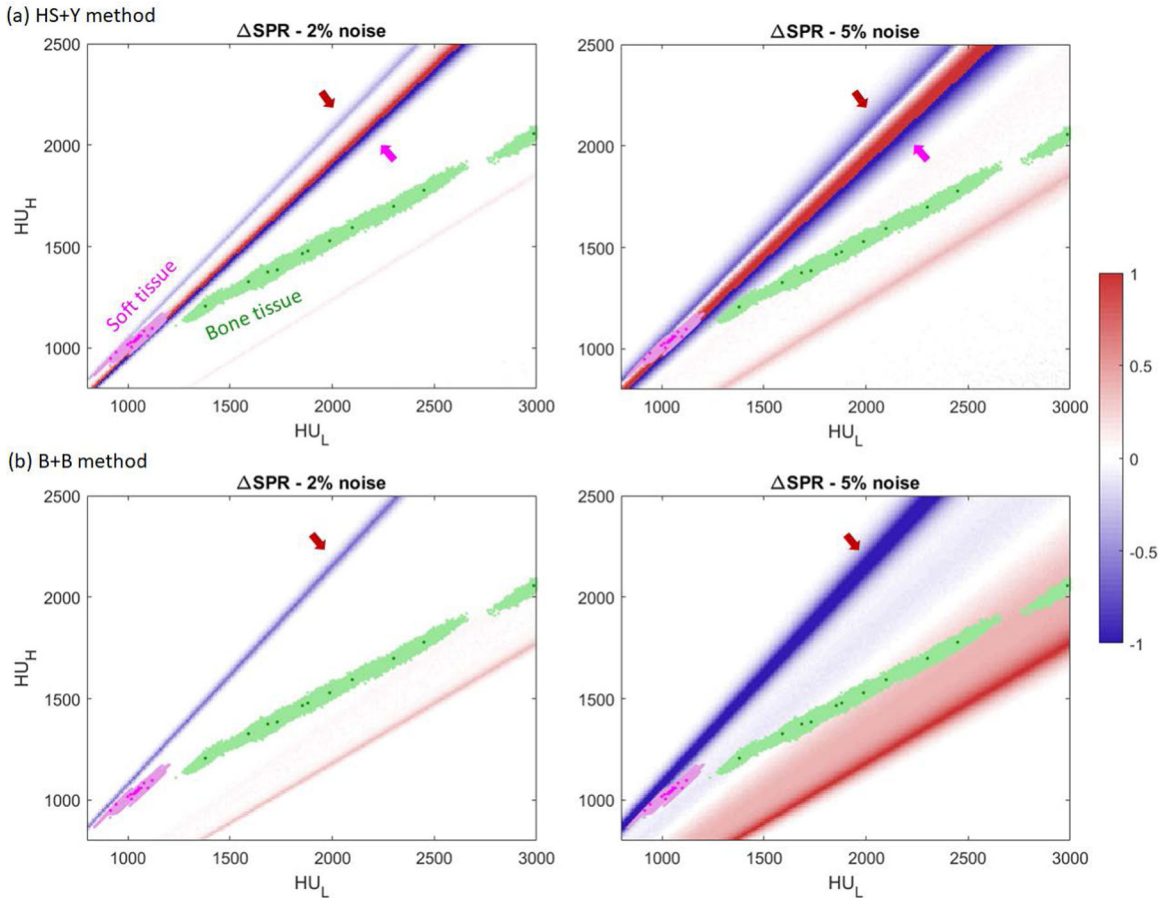

Figure 6.

Heatmap of the SPR mean shift (ΔSPR) using (a) the HS+Y method and (b) the B+B method at noise levels of 2% and 5%. Values are capped at [−1, 1] for ease of view as shown in the colorbar on the right. Grid size is 10×10. Magenta dots mark soft tissues and green dots mark bone tissues from the ICRU 44 reference. Shaded areas of each color denote 2000 individualized human tissue population. Arrows indicate the regions with hard threshold as shown in Fig. 4.

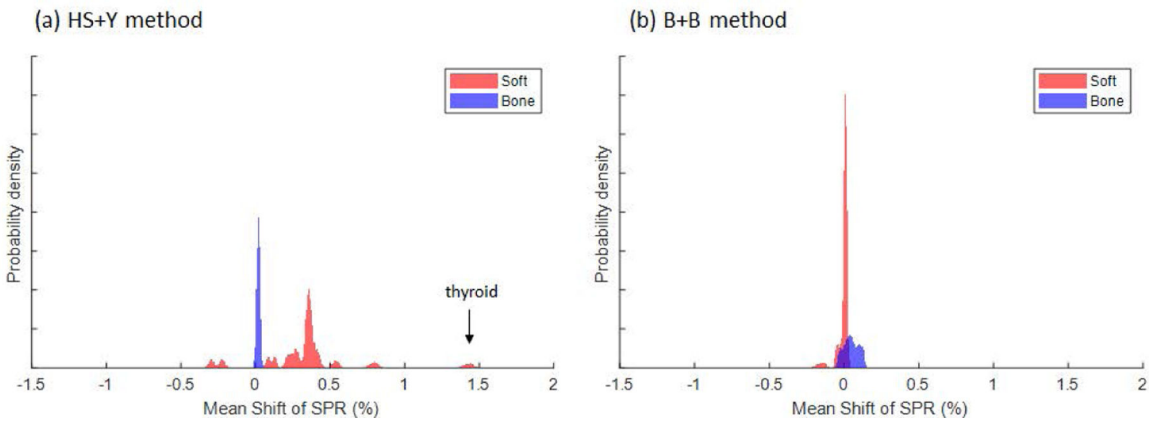

Figure 7.

Probability density function (PDF) of the mean shift for 2000 individualized human tissues using (a) the HS+Y method and (b) the B+B method at 2% noise. 23 soft tissues and 11 bone tissues were considered as is in the ICRU 44 reference.

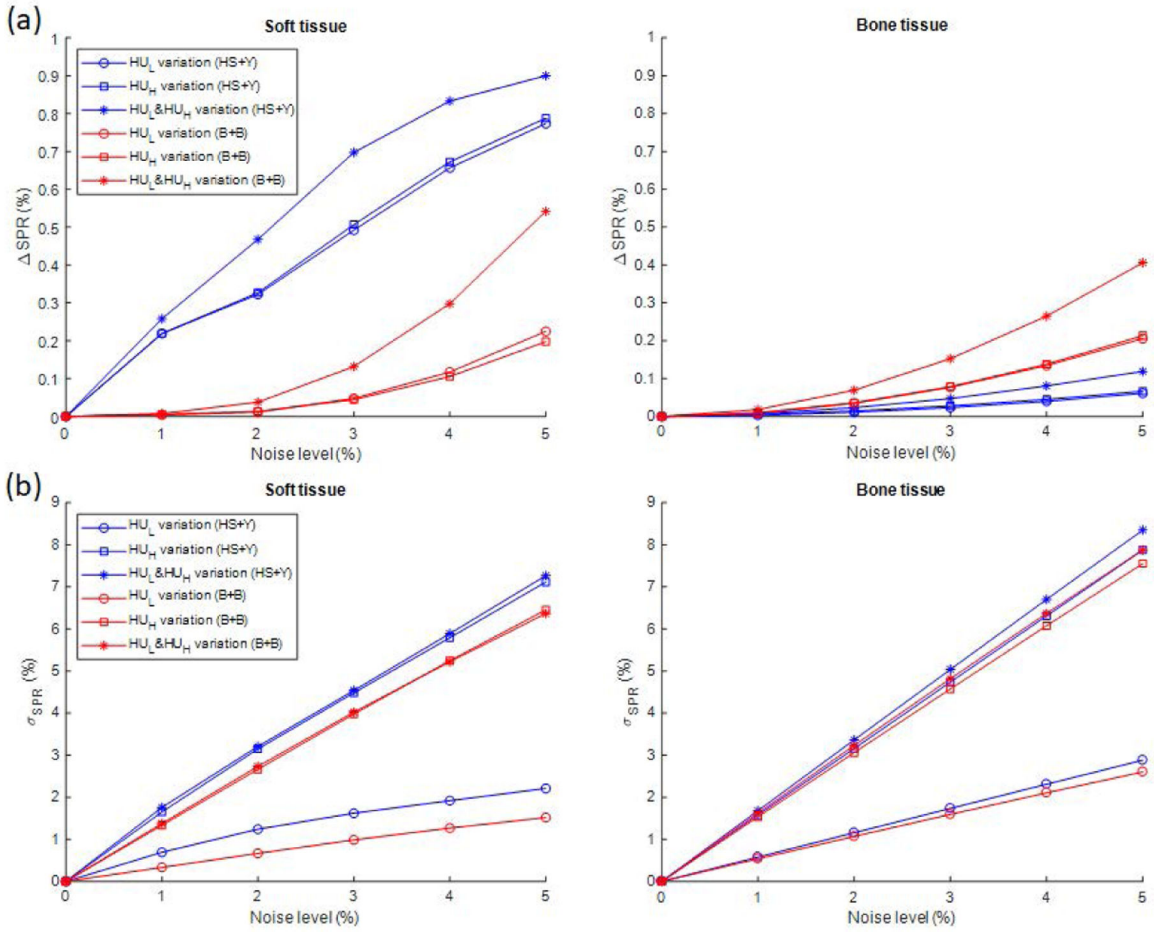

Figure 8.

Impact of noise on the SPR estimation manifested as (a) the shift of mean SPR (ΔSPR) and (b) the variation (σ_{SPR}) of SPR with varying levels of noise on HU_L, HU_H, or both. CT numbers from 2000 individualized human tissue samples were used.

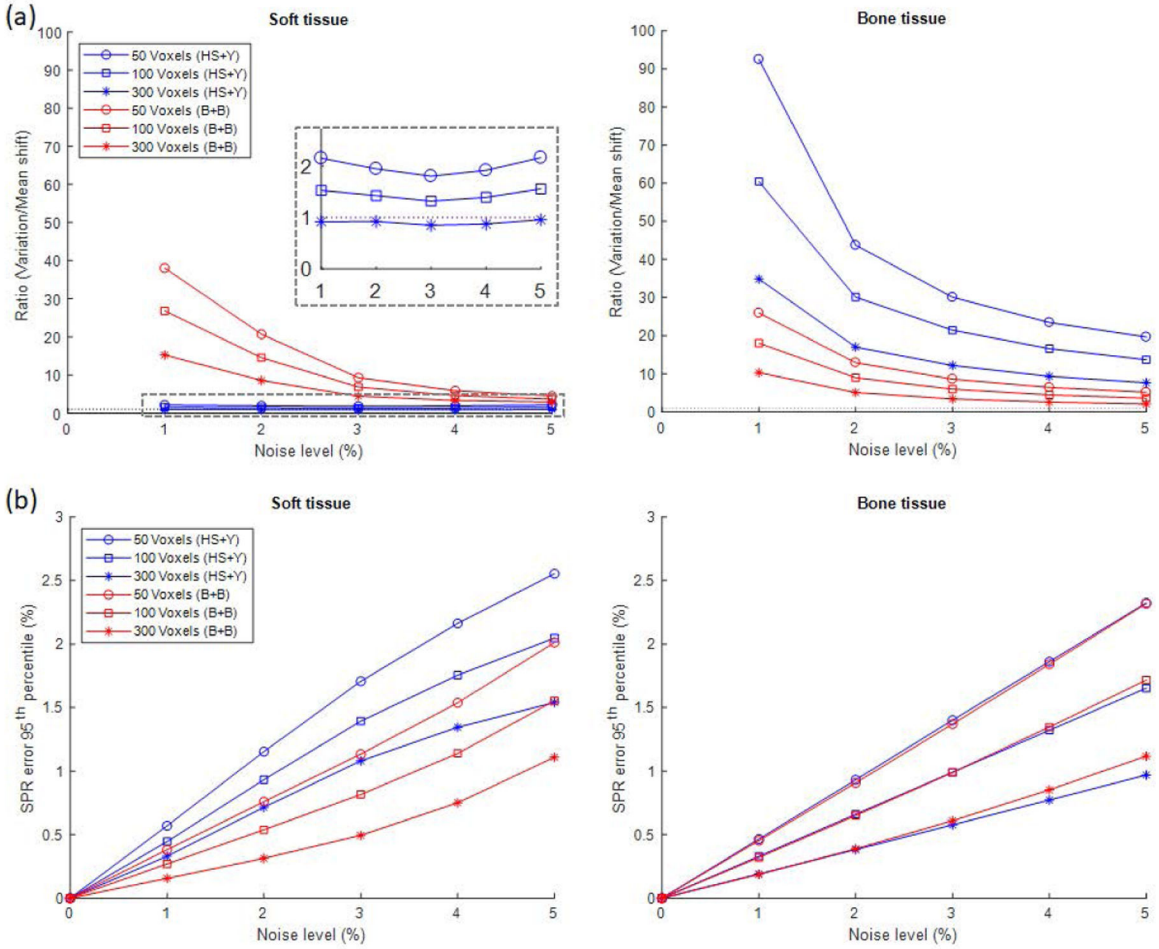

Figure 9.

Impact of noise on homogeneous tissues of specified number of voxels with varying levels of noise. (a) The ratio of the influence of the variation ($\sigma_{\mathrm{SPR}}/\sqrt{N}$, N is the number of voxels) vs. mean shift (ΔSPR). Gray dashed rectangle was magnified to visualize values near 1. (b) The range uncertainty (95$^{\mathrm{th}}$ percentile) resulting from the noise. Both HU_L and HU_H were added with Gaussian random noise.

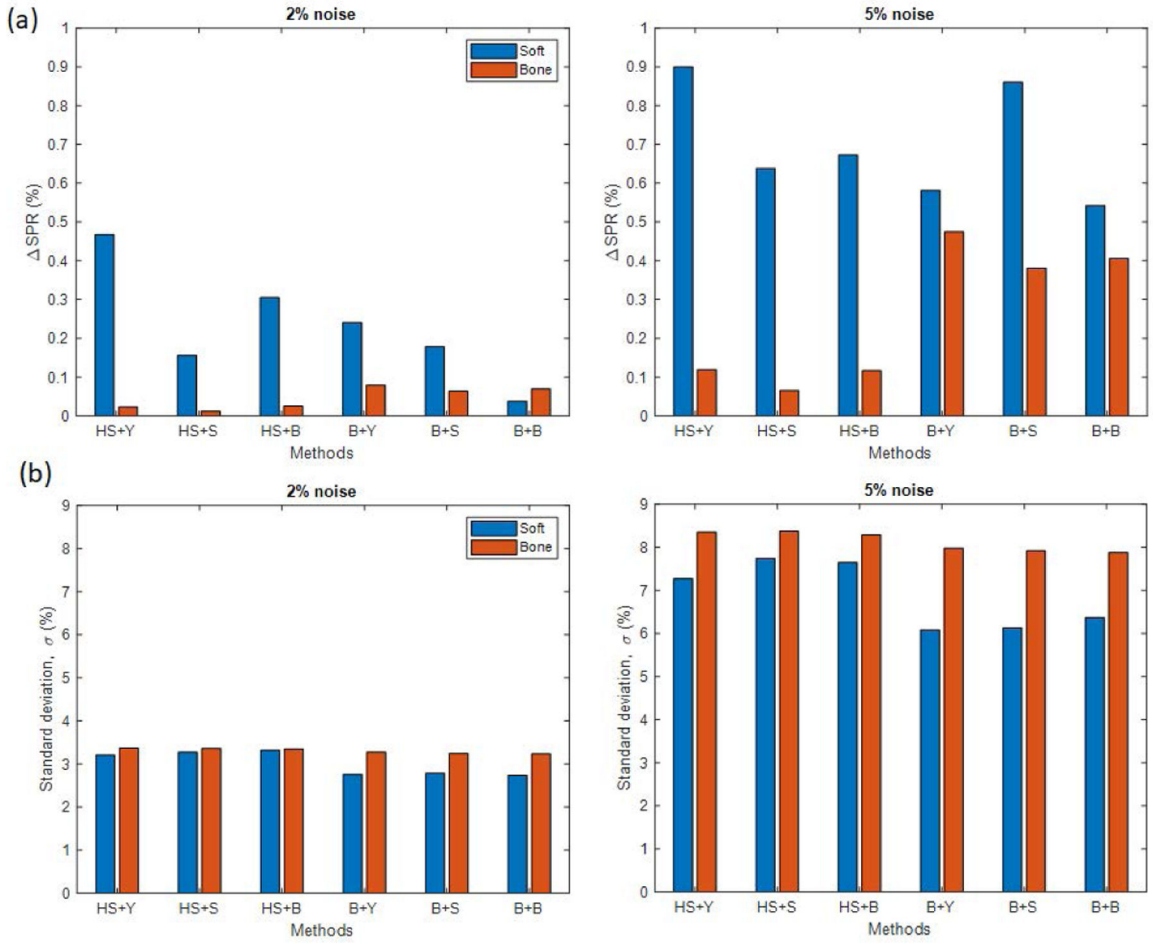

Figure 10.

Comparison of (a) SPR mean shift (ΔSPR) and (b) variation (σ_{SPR}) of SPR when using different combinations of methods for the calculation of ρ_e and Z (Hunemohr-Saito (HS) and Bourque (B)) and the conversion of Z-to-I (Yang (Y), Saito (S) and Bourque (B)). Two different noise levels (2% and 5%) were applied to both HU_L and HU_H. CT numbers from 2000 individualized human tissue samples were used.

Table 1.

Calibrated parameters for the HS method and the Bourque method (K=3 and M=6).

		Array index					
Method	**Parameter**	**1**	**2**	**3**	**4**	**5**	**6**
HS	a	−2.788E-01	1.271E+00	−7.593E-04			
	b	8.994E+03	−8.390E+03	1.563E+02			
Bourque							
	c	7.519E+00	3.941E+01	−4.017E+01			
	b_L	−1.125E+00	1.142E+00	−2.497E-01	2.633E-02	−1.288E-03	2.426E-05
	b_H	4.558E+00	−1.939E+00	4.096E-01	−4.216E-02	2.130E-03	−4.217E-05

Table 2.

List of ICRU 44 human tissues and calculated CT numbers using the HS method and the Bourque (B) method.

		80 kVp		150 kVp/Sn				80 kVp		150 kVp/Sn	
#	**Tissue**	**HS**	**B**	**HS**	**B**	**#**	**Tissue**	**HS**	**B**	**HS**	**B**
1	Adipose	915	904	949	955	18	Red Marrow	1012	1007	1027	1028
2	Blood	1065	1067	1059	1059	19	Yellow Marrow	942	930	979	987
3	Brain	1046	1046	1043	1043	20	Skin	1079	1076	1084	1084
4	Breast	999	993	1017	1018	21	Spleen	1063	1063	1060	1059
5	Cell Nucleus	1017	1022	1005	1005	22	Testis	1041	1041	1040	1040
6	Eye Lens	1053	1049	1061	1061	23	Thyroid	1099	1111	1060	1061
7	GI Tract	1028	1027	1031	1031	24	Skeleton-Cortical	2986	3031	2056	2050
8	Heart	1065	1066	1060	1060	25	Skeleton-Cranium	2300	2351	1698	1714
9	Kidney	1051	1051	1049	1049	26	Skeleton-Femur	1731	1776	1385	1403
10	Liver	1061	1062	1059	1058	27	Skeleton-Humerus	1988	2037	1529	1547
11	Lung (deflated)	1053	1054	1050	1049	28	Skeleton-Mandible	2448	2499	1778	1791
12	Lung (inflated)	248	261	257	260	29	Skeleton-Ribs (2nd, 6th)	1854	1901	1466	1485
13	Lymph	1036	1036	1034	1034	30	Skeleton-Ribs (10th)	2098	2148	1594	1612
14	Muscle	1050	1050	1048	1048	31	Skeleton-Sacrum	1590	1632	1327	1343
15	Ovary	1053	1053	1051	1051	32	Skeleton-Spongiosa	1380	1413	1207	1218
16	Pancreas	1037	1035	1041	1041	33	Skeleton-Vertebra (C4)	1881	1929	1478	1497
17	Cartilage	1120	1126	1097	1097	34	Skeleton-Vertebra (D6, L3)	1685	1729	1375	1392

Table 3.

Heterogeneous tissue distribution for three tumor sites.

	WEPL weight (%)			Voxel weight (%)		
Tumor site	**Lung**	**Soft**	**Bone**	**Lung**	**Soft**	**Bone**
Prostate	0.5	80.2	19.3	2.1	82.8	15.1
Lung	11.1	81.6	7.3	33.9	61.9	4.2
Head and neck	2.6	86.9	10.5	10	82.5	7.5

Table 4.

Range uncertainty (95th percentile) of homogeneous and heterogeneous tissues with 50 voxels.

	Range uncertainty (95th percentile)			
	HS+Y method		B+B method	
Tumor site	**2% noise**	**5% noise**	**2% noise**	**5% noise**
Homogeneous				
Soft	1.15	2.55	0.76	2.01
Bone	0.93	2.32	0.91	2.32
Heterogeneous				
Prostate	1.04	2.42	0.81	1.99
Lung	1.17	2.68	0.86	2.21
Head and neck	1.09	2.48	0.81	2.04